Numerical Modelling and Theoretical Analysis of Timber-Concrete Glued-in Threaded Rod Shear Connectors with and without Notches

Chao Yang, a,* Zhibin Ling, b Zheng Li, c Zhiqiang Qin, d and Jie Shen a

Timber-concrete composite (TCC) structures offer superior bending stiffness, load capacity, and environmental benefits, but shear connector performance—critical for timber-concrete integration—remains a challenge. This study investigated TCC structures using notched shear connectors and glued-in threaded rods (GiRs) via push-out tests, finite element (FE) modelling, and parametric analyses. Twenty-seven specimens were tested, and the validated FE model simulated material nonlinearities and contact. The results showed increased GiR diameter and embedment length enhance load capacity and stiffness (GL series), with diminishing returns beyond a certain embedment. A 100 mm notch size optimized stiffness and load capacity for notched connectors (RG series). Parametric studies highlighted the influence of notch size, GiR embedment length, and diameter on load capacity, stiffness, and ductility. The FE model accurately predicted structural behavior, and theoretical models for load capacity prediction showed 1 to 32% error. This study provides valuable insights for optimizing TCC shear connector design and enhancing structural performance.

DOI: 10.15376/biores.20.4.10460-10486

Keywords: Finite element; Push-out tests; Timber-concrete composite; Shear connectors; Glued-in rod

Contact information: a: College of Mechanical and Electrical Engineering, Northeast Forestry University, Harbin 150040, China; b: School of Civil Engineering, Suzhou University of Science and Technology, Suzhou 215011, China; c: College of Material Science and Engineering, Northeast Forestry University, Harbin 150040, China; d: School of Civil Engineering and Transportation, Northeast Forestry University, Harbin 150040, China; * Corresponding author: yangchaoedc@163.com

INTRODUCTION

Timber-concrete composite (TCC) structures, which strategically integrate dissimilar materials to maximize their individual advantages, have gained widespread adoption in recent years for applications ranging from the retrofitting of existing timber floors to new construction projects and bridge systems (Djoubissie *et al.* 2018). Life Cycle Assessment (LCA) studies using standard tools (*e.g.*, SimaPro 9.0) have shown that TCC structures exhibit 30 to 40% lower embodied carbon per kN load capacity compared to steel-concrete composite structures (Rodrigues *et al.* 2017; Eslami 2023). This advantage stems from the renewable nature of timber and lower energy consumption during glulam production. A typical TCC system includes a concrete slab, a timber beam under tension and bending, and shear connectors (Di Nino *et al.* 2020). Compared to timber floors, TCC floors offer greater stiffness, load capacity, and better insulation, while protecting timber from climate effects. Compared to reinforced concrete floors, TCC floors reduce weight and construction time (Dias *et al.* 2015).

The shear connector is crucial for integrating timber and concrete in composite systems, determining both performance and installation feasibility. Extensive prior research has focused on optimizing connector geometries and associated parameters to enhance the performance of TCC systems. Research has explored various connectors such as nails (Ahmadi and Saka 1993), screws (Quang Mai et al. 2018; Derikvand and Fink 2022), bolts (Cao et al. 2021a), reinforcement bars (Dias et al. 2007a; Djoubissie et al. 2018), steel tubes (Gurkšnys et al. 2005; Fragiacomo and Lukaszewska 2013), steel plates (Shi et al. 2021; Shahnewaz et al. 2022; Zeman et al. 2024), notches (Boccadoro and Frangi 2014; Boccadoro et al. 2017) and hybrid connections (Ling et al. 2022; Shi et al. 2022; Zhang et al. 2022; Ling et al. 2023). The adoption of metal-type connections, while contributing to the ease of construction, does not effectively utilize the function of bonding concrete to timber. Dias et al. (2011) proposed a maximum spacing that should be allowed to optimize the performance of TCC systems by comparing the ductility and load-bearing capacity of notch connections, glued connections, and metal-based connections. Although the approach can somewhat balance the ductility and load carrying capacity of the structure, the results showed that the approach is limited. Boccadoro and Frangi (2014) has proved that TCC notch connection can effectively reduce the construction cost and ensure the composite efficiency through six sets of four-point bending tests with different notched connection forms. However, although the composite efficiency is excellent, the brittle failure mode still requires careful attention.

Hybrid connector configurations, combining metal-based connections (which offer superior ductility but lower stiffness and load capacity) with notched connections (which provide inferior ductility but higher stiffness and load capacity), have garnered increasing attention. Yeoh *et al.* (2011) conducted 30 double shear push-out tests, including notched connections with lag screws and steel toothed plates. The notch length enhanced connection strength, lag screws improved post-peak behavior and ductile failure, and a 300 mm notch with lag screws was 3× stronger and 8.5× stiffer than un-notched lag-screw-only connections. Notched connections with lag screws avoided brittle failure, unlike abrupt steel toothed-plate failures. Deam *et al.* (2007) evaluated the stiffness, strength, and ductility of various connections using asymmetric shear tests, demonstrating that rectangular notches with screw reinforcement performed optimally. Their research showed that rectangular concrete notches reinforced with cruciform screws at 500 mm spacing enabled composite action for 8 m spans. Djoubissie *et al.* (2018) analyzed connections formed by notched and threaded bars; these hybrid configurations combined the stiffness advantages of notched connections with the ductility benefits of steel connections.

While notch-dowel connections demonstrated adequate composite efficiency in numerous cases, the embedded timber regions and timber-concrete bond performance often remained suboptimal, with certain configurations inducing initial timber damage during installation. To investigate how different fixation methods affect joint performance, Molina et al. (2020) compared reinforcement bar connections installed via epoxy adhesion versus those inserted into undersized timber holes (without adhesive bonding). Their results indicated that epoxy-bonded rebar connections exhibited superior stiffness and strength compared to friction-fit alternatives, highlighting the importance of mechanical fixation strategies on overall connection performance.

In addition to the studies mentioned above, numerical modeling, especially finite element (FE) analysis, has been used to simulate the behavior of TCC system under different loading conditions. Dias *et al.* (2007b) developed a numerical model for simulating TCC dowel connections. However, the simplified wood constitutive model

enabled accurate prediction of load-slip behavior but simultaneously overestimated maximum load capacities and initial stiffness values. Oudjene *et al.* (2013) introduced a beam-solid FE model for analyzing the nonlinear behavior of screw-type TCC connections. While effective for load-slip behavior prediction, this approach neglected metal fastener failure mechanisms and provided limited insight into failure mode transitions through parametric analyses. Bedon and Fragiacomo (2017) employed idealized elastoplastic constitutive relationships with cohesive zone elements to predict the nonlinear behavior of TCC notched joints. While their model accurately predicted failure loads and modes, it significantly overestimated ultimate tangent stiffness values, highlighting the need for improved material characterization in numerical simulations.

Numerous studies have explored the behavior of TCC shear connectors, yet challenges remain in understanding the influence of various parameters on their load capacity, stiffness, and ductility, and in accurately predicting their performance across different configurations. Recent advances in composite structure analysis have highlighted the value of reliability-based modeling (Harrach et al. 2022) and hybrid material reinforcement (Khaleel Ibrahim et al. 2023). These works emphasize the integration of advanced modeling techniques with multi-material synergy, providing a relevant framework for the present study—which combines GiR (metal) and notched (timberconcrete) connections to optimize TCC performance through experimental and FE approaches. This study aims to address these gaps by investigating the performance of TCC structures with notched shear connectors and glued-in threaded rods (GiR) through experimental push-out tests, three-dimensional finite element modeling, and parametric analyses. A schematic diagram of the connection is shown in Fig. 1. The main objectives were to develop a validated FE model to predict the structural behavior of TCC connectors, analyze the effects of key parameters such as notch size, GiR diameter, and embedment length on connector performance, and propose theoretical models for load capacity prediction. This study provides valuable insights for optimizing TCC shear connector design and enhancing structural performance.

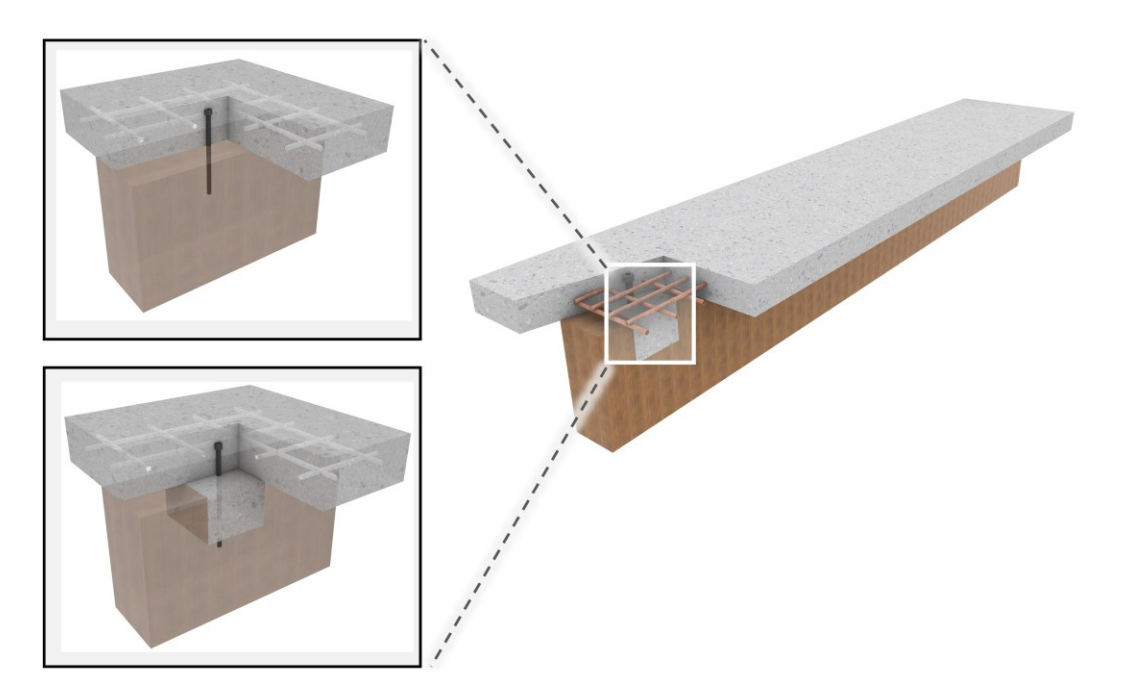


Fig. 1. The schematic diagram of the GiR connection and notched shear connectors

EXPERIMENTAL

Push-out Test

A systematic and comprehensive series of push-out tests was conducted on GiR connections, evaluating both configurations with and without notched connectors. The detailed specimen geometries and specific configurations are summarized in Table 1 and illustrated in Fig. 2. Each push-out test specimen was designed with a symmetrical threelayer structural arrangement, comprising two reinforced concrete slabs enclosing a glued laminated timber (GLT) beam. The GLT was manufactured from Norway spruce (Picea abies) (a commonly used structural softwood), with a strength class of C24 per EN 338 (1995) (density = 420 kg/m³, longitudinal compressive strength = 35.5 MPa). The GLT's grain orientation was parallel to the beam's length direction (longitudinal axis), as labeled in Fig. 1 (d), to ensure alignment with the primary bending/tension forces in TCC beams. The GLT dimensions were 130 mm (width) \times 360 mm (height) \times 400 mm (length), with lamella thicknesses of 30 mm (bonded with structural epoxy adhesive). To enhance structural performance, steel meshes were embedded within the concrete slabs, consisting of 8 mm-diameter HRB400 reinforcement bars (yield strength = 400 MPa) arranged in a bidirectional pattern (longitudinal and transverse directions). The bar spacing was uniformly set to 100 mm × 100 mm (center-to-center), conforming to the minimum reinforcement requirements of EN 1992-1-1 (2005) for structural concrete slabs. The mesh was placed 20 mm from the slab surface (cover depth) to prevent corrosion. The GiR connectors were installed into the timber beam using a thin 1 mm adhesive layer to ensure proper bonding. A structural nut was securely fastened at the top of each threaded steel rod to improve the anchorage mechanism within the concrete slab, thereby enhancing the overall load transfer capacity of the connection.

Table 1. Geometry and Details of the Tested TCC Connector for GiR with and without Notch Connections

Specimen code	d (mm)	I (mm)	I _c (mm)	In (mm)	h (mm)	Number of replicates
GL10-150	10	150	50	-	-	3
GL12-170	12	170	50	-	-	3
GL16-210	16	210	50	-	-	3
RG12-50	12	170	100	50	50	3
RG12-100	12	170	100	100	50	3
RG12-150	12	170	150	150	50	3

Note: d is the nominal diameter of GiR, l is the total length of the GiR, l_c is the embedment length of the GiR within the concrete, l_n is the length of notch, and h is the height of notch.

A high-precision force transducer (model: HBM U9C) with a range of 0 to 500 kN and precision of $\pm 0.1\%$ full scale (FS) was installed between the testing machine and the specimen to measure applied load. Furthermore, four linear displacement transducers (model: Keyence GT2) with a range of 0 to 50 mm and precision of ± 0.01 mm were positioned at critical locations (e.g., timber-concrete interface corners) to capture maximum relative slip, as these regions are most representative of the deformation behavior of the specimens.

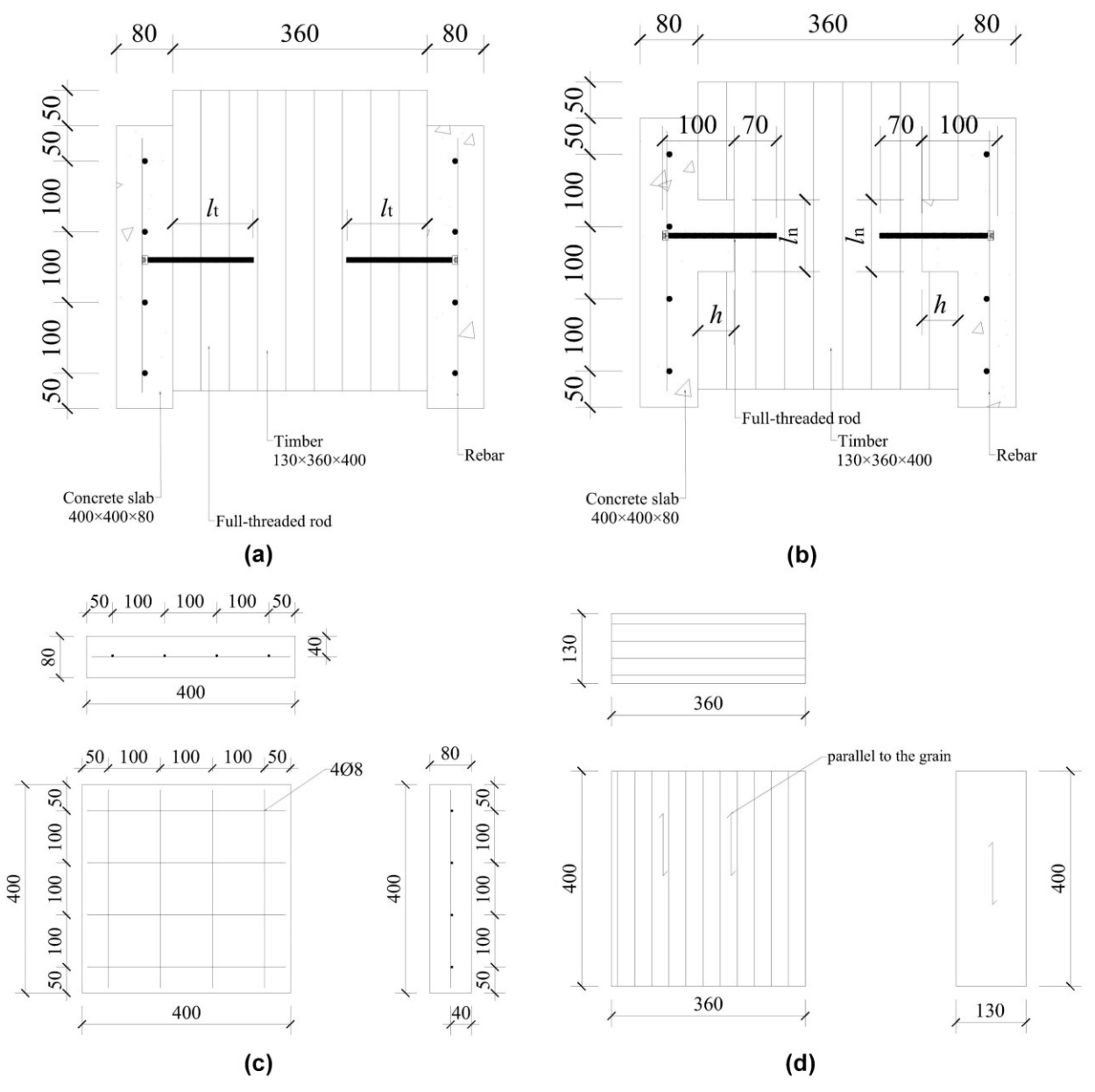


Fig. 2. TCC push-out specimens for GiR with and without notch connections (all dimensions in mm): (a) GL series configuration (no notch), showing full-threaded GiR (d = 10-16 mm), timber beam (130 × 360 × 400 mm), and concrete slabs (400 × 400 × 80 mm); (b) RG series configuration (with notch), adding a notch ($I_n = 50-150$ mm, h = 50 mm) at the timber-concrete interface; (c) cross-section of the reinforced concrete slab, showing 8 mm-diameter rebar mesh (spacing = 100 mm × 100 mm); and (d) cross-section of the glued laminated timber component.

The specific arrangement of these transducers is illustrated in Fig. 3(a). The final specimen displacement was determined as the average of these relative displacement values. This multi-transducer configuration facilitated comprehensive monitoring of both force transmission and deformation characteristics during the push-out tests, thereby providing reliable data for subsequent analysis of connection behavior. The loading protocol strictly conformed to the standardized procedures specified in EN 26891 (1991), as shown in Fig. 4. To prevent overturning during loading, angle steels and tie rods were installed on both sides of the specimen.

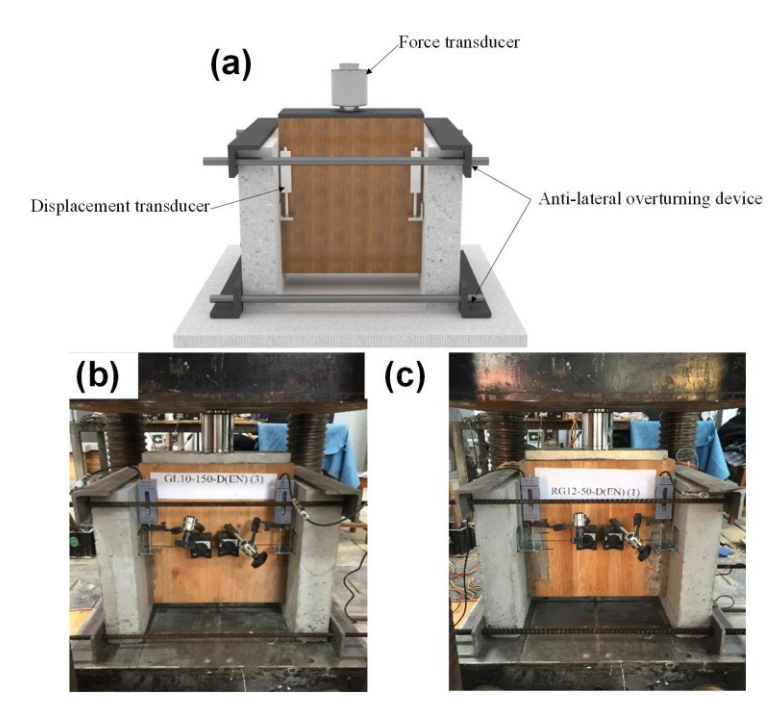


Fig. 3. Test set-up of TCC push-out specimens for GiR with and without notch connections: (a) diagram of the measuring and loading device; (b) GL series shear connector loading graph; and (c) RG series shear connector loading graph

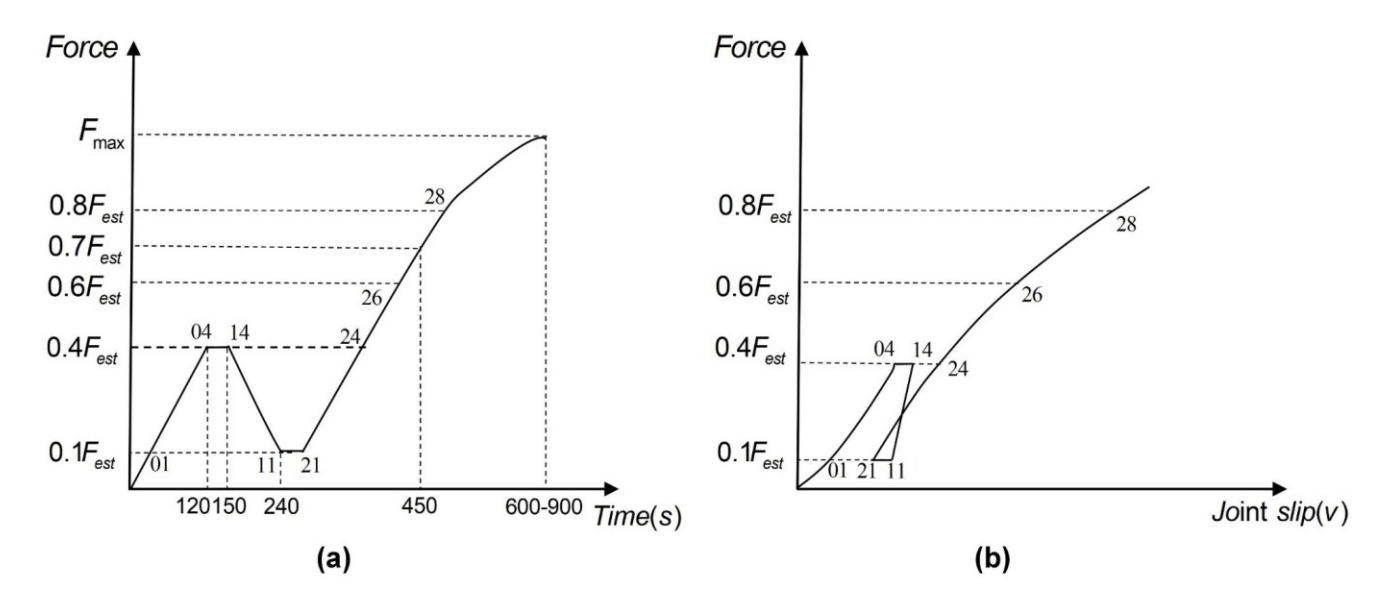


Fig. 4. Loading regime of EN 26891 (1991) and the corresponding load-slip curve

Numerical Model

A three-dimensional FE model in the Abaqus CAE/Standard 2020 (Abaqus User Manual 2021) was developed. Reinforced concrete slabs, glulam, and GiR with a nut were taken into consideration for the FE modelling. The material nonlinear properties and contact nonlinearities of timber as well as concrete were also considered to ensure effective failure mode prediction.

RESULTS AND DISCUSSION

Material Properties and Constitutive Laws

The constitutive model of a material serves as the most critical factor determining the accuracy of numerical simulations, making the rational selection of a constitutive relationship that can precisely characterize material behavior essential to the validity of this study. In TCC connectors, three fundamentally different materials are involved: timber, reinforced concrete, and metal shear members. The improper selection of a constitutive relationship for any of these materials could significantly undermine the reliability and accuracy of the simulation results. The constitutive relationships utilized in this study incorporated well-established methodologies from previous research while introducing specific modifications tailored to the unique requirements of this investigation.

Timber

Several yield criteria have been employed to simulate the stress-strain relationships of timber material properties, including the Tsai-Wu criterion (Mascia and Nicolas 2012), Yamada-Sun criterion (Mohamadzadeh *et al.* 2012), and Hoffman criterion (Eslami *et al.* 2021). The Hill-potential method implemented in Abaqus has been demonstrated to effectively predict the mechanical behavior of timber composite structures (Ling *et al.* 2022; Chen *et al.* 2025).

This study adopted the Hill criterion as the constitutive model for timber material characterization. The constitutive modeling approach presented herein treats wood as an anisotropic material under Hill's criterion, with identical mechanical properties assumed for both tension and compression loading conditions. While this simplification may lead to deviations from actual behavior when forces are applied perpendicular to the grain, the study focuses on radial compression as the predominant loading scenario. Under these conditions, the isotropic assumption regarding tension and compression is considered to have minimal impact on the predictive accuracy of the model. The elasticity parameters are shown in Table 2. The Young's modulus and shear modulus values were determined based on the theoretical relationship established by Bodig and Jayne (1982), with additional implementation details available in Ling *et al.* (2018). The plastic parameters calculated according to Hill's criterion and EN 338 (1995) are shown in Tables 3 and 4. The specific calculation formula is shown in Eq. 1,

$$R_{11} = \frac{\overline{\sigma}_{11}}{\sigma^0}, R_{22} = \frac{\overline{\sigma}_{22}}{\sigma^0}, \quad R_{33} = \frac{\overline{\sigma}_{33}}{\sigma^0}, \quad R_{12} = \frac{\sqrt{3}\overline{\sigma}_{12}}{\sigma^0}, \quad R_{13} = \frac{\sqrt{3}\overline{\sigma}_{13}}{\sigma^0}, \quad R_{23} = \frac{\sqrt{3}\overline{\sigma}_{23}}{\sigma^0}$$
(1)

where σ^0 is the yield stress that defines the material entering the plastic stage, which is taken as the longitudinal compressive strength of timber. The parameter σ_{ij} is the yield stress value measured in each direction, which is taken as the compressive strength and shear strength of the timber in each direction.

 Table 2. Material Properties for GLT in Elasticity

Modulus	Modulus of Elasticity (MPa)			Poisson's Ratio			Shear Modulus (MPa)			
E ₁₁	E 22	E 33	v_{12}	v_{13}	v_{23}	G ₁₂	G 13	G 23		
12800	1024	640	0.37	0.43	0.63	914	859	91		

Table 3. Material Properties for GLT in Plasticity

Compressive Yield Stress (MPa)			Tensile Strength (MPa)			Shear Yield Stress (MPa)			
L	R	Т	L	R	T	L	R	Т	
35.5	5.25	5.05	35.5	5.25	5.05	35.5	5.25	5.05	

Note: T =tangential, R =radial and L =Longitudinal direction

Table 4. Input Parameters of the Hill Yield Criterion in ABAQUS

R ₁₁	R ₂₂	R ₃₃	R ₁₂	R ₁₃	R ₁₁
1	0.148	0.142	0.4	0.36	0.36

Reinforced concrete

The elastic-plastic behavior of concrete in this study was determined based on the calculation methods outlined in Eurocode 2 (EN 1992-1-1 2005), incorporating experimental data from concrete specimen material property tests. The elastic modulus ($E_{\rm cm}$) of the concrete was calculated using Eq. 2.

$$E_{\rm cm}(\text{GPa}) = 22 \times [(30.01)/10]^{0.3} = 30.5 \text{ (GPa)}$$

The Concrete Damaged Plasticity (CDP) model, originally proposed by Lee and Fenves (1998), is an advanced material model integrated within the Abaqus FE software specifically designed to simulate the nonlinear mechanical behavior of concrete. This model has been extensively validated and demonstrated its effectiveness in accurately predicting the mechanical response of concrete under various loading conditions, as evidenced by recent studies (Hassanieh *et al.* 2018; Tao *et al.* 2022).

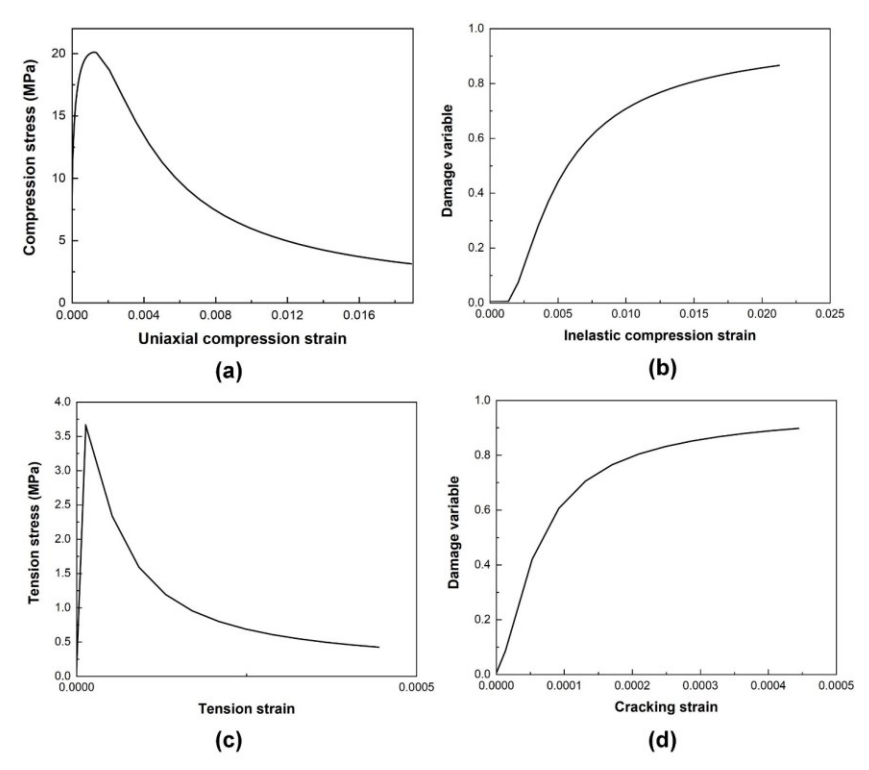


Fig. 5. The material behavior for concrete: (a) stress-strain under compression; (b) evolution of compressive damage; (c) stress-strain under tension and (d) evolution of tensile damage

The plasticity parameters were selected in accordance with the recommendations of Jankowiak and Lodygowski (2005) for the flow potential eccentricity e = 0.1 and dilatancy angle w = 31. A biaxial to uniaxial compressive strength ratio of 1.16 was adopted, as specified in the Abaqus User Manual (2021). The details are shown in Table 5. The resulting stress-strain relationships under both tension and compression, along with the progression of damage development with increasing inelastic strains, are presented in Fig. 5.

Table 5. Material Properties for Concrete

<i>E</i> (GPa)	Poisson's Ratio	Dilation Angle	Eccentricity	$f_{ t b0}/f_{ t c0}$	К	Viscosity Parameter
30.5	0.2	31	0.1	1.16	0.67	0.005

GiR and rebar

For the GiR components and reinforcing bars, the elastic isotropic plastic hardening material model was employed to describe their mechanical behavior. The GiR components were fabricated from Grade 8.8 steel, which exhibits a minimum yield strength of 600 MPa for the GiR and 800 MPa for the nuts, respectively. The reinforcing bars utilized HRB400 steel with a defined yield strength of 400 MPa. Across all steel components, the elastic modulus and Poisson's ratio were standardized at 206 GPa and 0.3, respectively. The corresponding uniaxial tensile stress-strain curves are illustrated in Fig. 6.

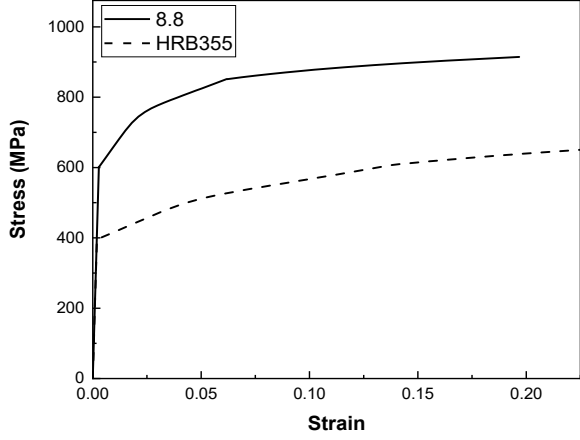


Fig. 6. Uniaxial stress-strain curves for Grade 8.8 and HRB355 steel

Contacts, Loading, Boundary Conditions, and Analysis Procedure

The FE model employed in the analysis was constructed using a 1/4 symmetry model to optimize computational efficiency while maintaining accuracy. To establish a stable support condition, all degrees of freedom (DoFs) at the bottom surface of the concrete specimen were fully constrained. Displacement-controlled loading was applied at the top surface of the GLT to simulate the push-out test conditions. Symmetry boundary conditions were imposed on the remaining lateral surfaces to ensure that both displacement and rotational degrees of freedom adhered to symmetry requirements, thereby enhancing the reliability of the simulation results. The specific boundary conditions are illustrated in in Fig. 7 (a). The contact interactions within the model are defined as follows: At the interface between GLT and concrete, a hard contact formulation was employed with a friction coefficient of 0.1 to characterize their mechanical interaction. For the GLT-GiR

interface, a cohesive contact approach was utilized to accurately capture the bonding-slip behavior observed in this material combination. This modeling strategy has been validated as effective in previous studies (Azinović *et al.* 2019; Shirmohammadli *et al.* 2023).

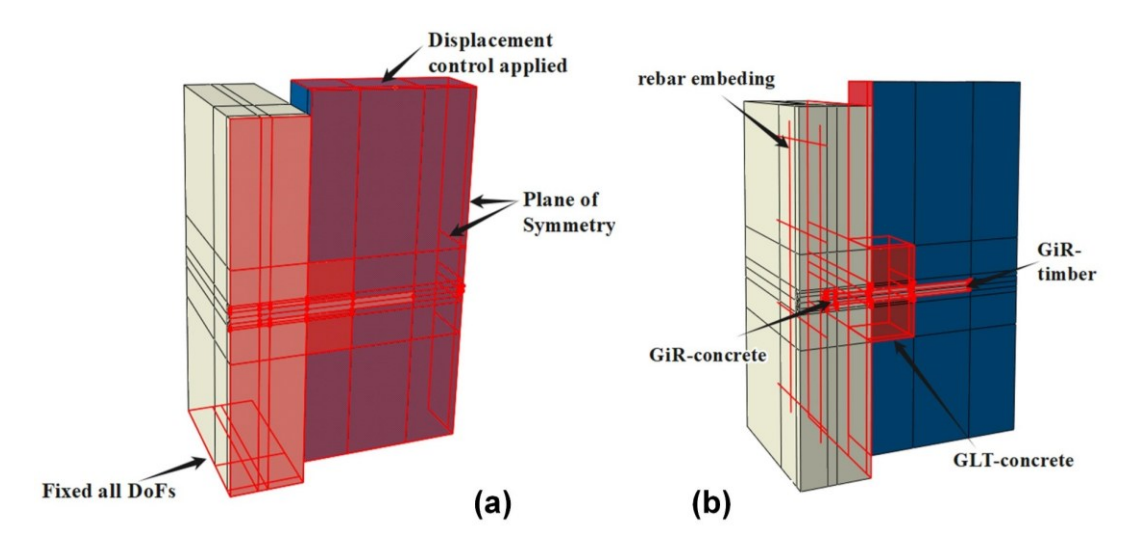


Fig. 7. (a) Boundary conditions and (b) interface/contact conditions in the finite element models

Table 6. Cohesive Contact interface Parameters

	K _{nn}	<i>K</i> _{tt,1}	<i>K</i> tt,2	σ	τ ₁	τ2	δ_{f}	η
	(N/mm ³)	(N/mm ³)	(N/mm ³)	(MPa)	(MPa)	(MPa)	(mm)	
Timber-	1300	500	500	5	8.5	8.5	0.3	0.005
adhesive of rod								

Note: K_{nn} is the stiffness in the normal direction (Azinović *et al.* 2019; Danielsson *et al.* 2019), $K_{tt,1}$ and $K_{tt,2}$ are the stiffness in the shear directions (Azinović *et al.* 2019; Danielsson *et al.* 2019), σ is the strength in the normal direction, limited by the perpendicular to the grain tensile strength of timber. τ_1 and τ_2 are the shear strengths (Serrano 2001; Azinović *et al.* 2019), δ_f is the displacement at failure, taken from test experience, and η is the viscosity coefficient.

The specific cohesive behavior parameters adopted in this study are detailed in Table 6. In the initial modeling phase, a 1mm-thick adhesive layer was explicitly modeled between GLT and GiR. However, subsequent analyses demonstrated that the influence of this adhesive layer thickness on the overall model response was negligible (Initial comparison results were provided in the appendix, where FE-Adhesive represents the solid adhesive layer modeling). Consequently, the explicit solid modeling of this adhesive layer was omitted in the final model configuration. For the concrete-GiR interface, a hard contact condition with a higher friction coefficient of 0.5 was specified to account for the different material interaction characteristics. Additionally, the reinforcement bars were integrated into the concrete matrix using Abaqus's built-in "embedding" feature, which ensures proper load transfer between the reinforcement and surrounding concrete while maintaining computational efficiency.

Element Type and Mesh

The mesh size for the concrete panels and GLT was restricted to 10 mm in the vicinity of the GiR surface, while in the remaining areas it was maintained below 20 mm. The rebar mesh was similarly specified with a 10 mm size to promote numerical

convergence. For threaded rods, the mesh size along their length was set to 5 mm, whereas the mesh in the circular cross-section direction was determined by the number of divisions, with four units per split edge. All components, excluding the reinforcement, were meshed using 8-node hexahedral elements (Fig. 8) with a full integration scheme to ensure precise stress and strain calculations. The reinforcement bar was modeled using 'beam' elements to accurately capture its ability to carry shear forces and ensure proper load transfer within the structure.

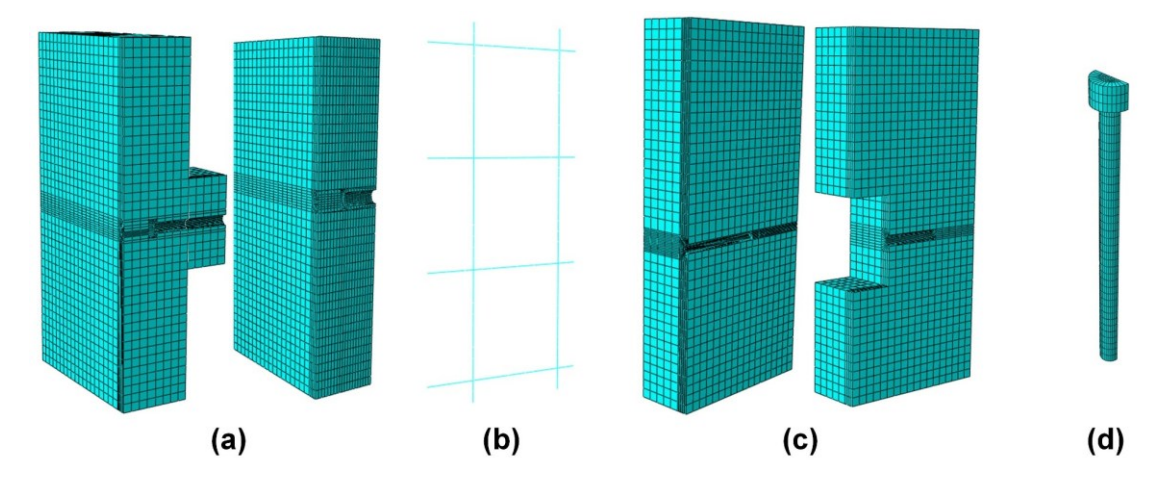


Fig. 8. Outline of the FE mesh and adopted mesh size for (a) concrete, (b) reinforced rebar, (c) GLT, and (d) threaded rod

Verification and Validation of the FE Model

The FE model was verified and validated through comprehensive comparisons between the simulated load-slip curves and the experimentally observed failure modes. For the GL series specimens (Figs. 9 (a)-(c)), the FE model exhibited excellent agreement with the experimental results, effectively replicating the overall trends of the load-slip behavior.

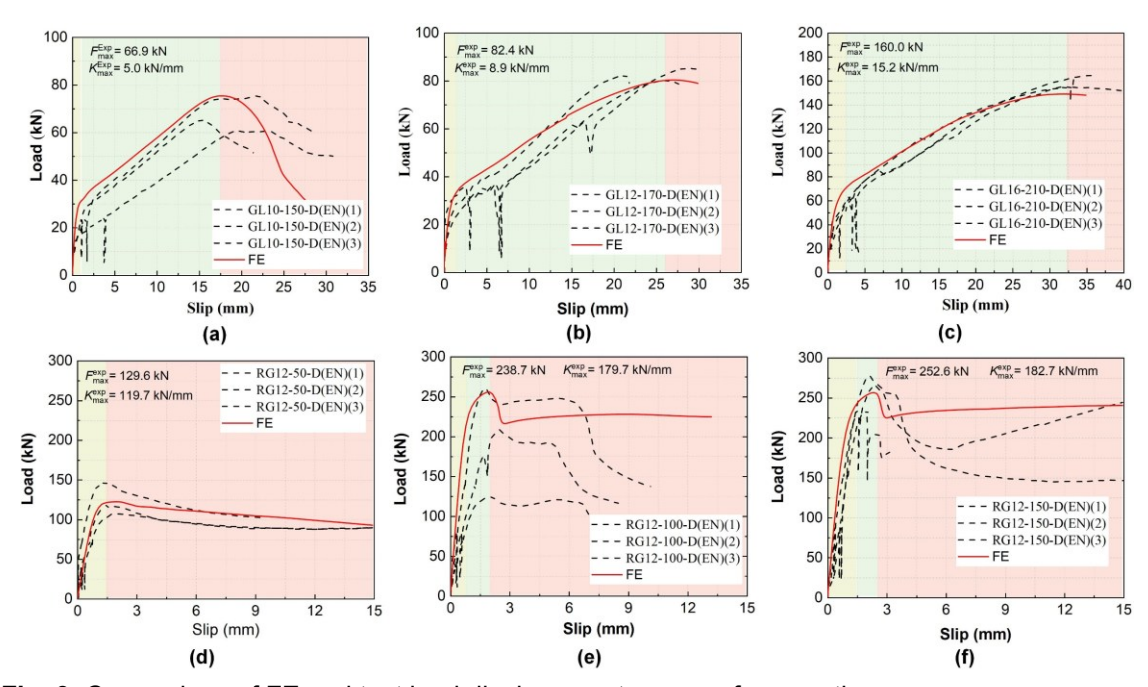


Fig. 9. Comparison of FE and test load displacement curves of connections

During the initial loading phase, both the numerical predictions and experimental measurements demonstrated a linear increase in load with respect to slip displacement. Upon attainment of the peak load, the curves transitioned into a nonlinear softening phase, which was accurately captured by the FE model. Nevertheless, minor discrepancies were noted in the post-peak region, which may be attributed to localized damage mechanisms such as concrete crushing and steel yielding at the interfaces—phenomena that might not be fully accounted for in the current FE simulation. Similarly, for the RG series specimens (Figs. 9 (d)-(f)), the FE model demonstrated good agreement with the experimental data. The simulated load-slip curves exhibited a linear elastic phase followed by a nonlinear softening phase, closely matching the experimental observations. The observed deviations in the post-peak load softening behavior can be attributed to the intricate interaction between steel and concrete components, as well as the inherent simplifications in modeling the bond-slip behavior within the FE framework. The more specific test data can be found in the appendix.

The failure modes observed in the experimental tests were also compared with the FE results. Figure 10 depicts the distribution of force and deformation within the specimens during both testing and simulation, providing a comprehensive visualization of their behavior.

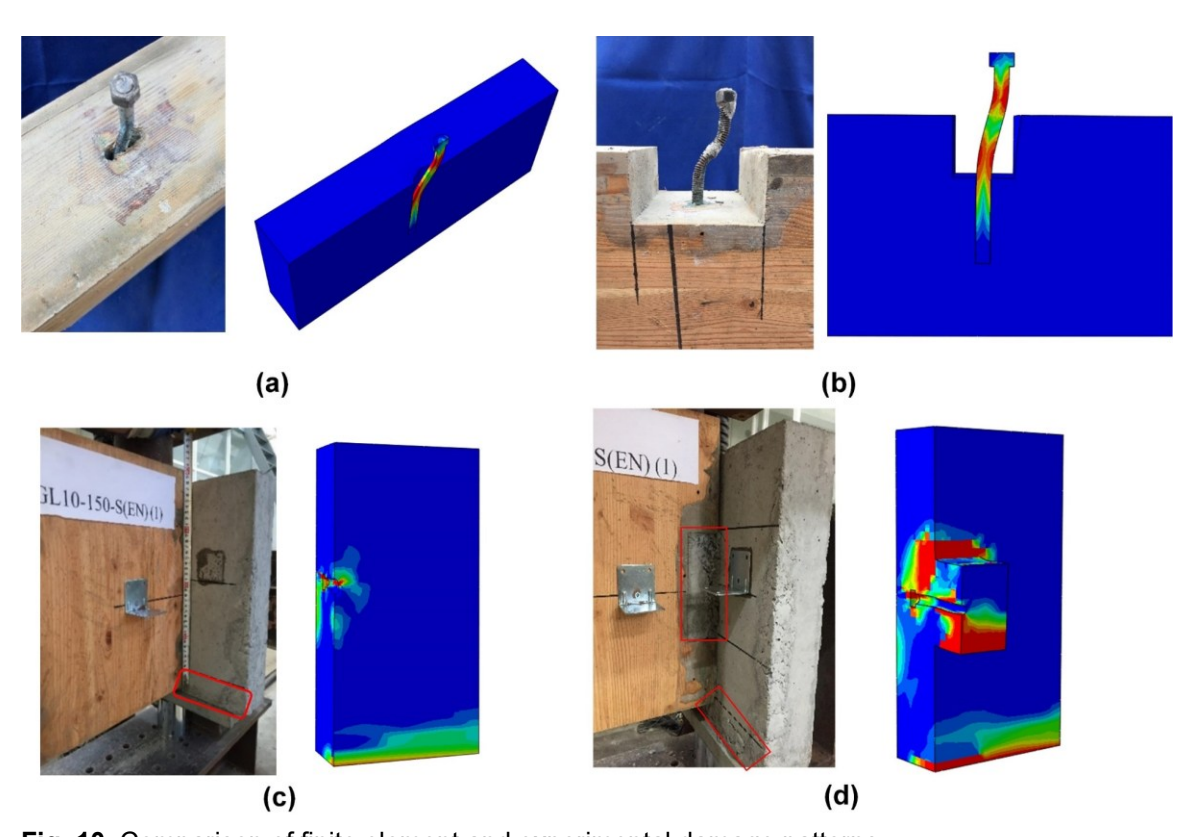


Fig. 10. Comparison of finite element and experimental damage patterns

The experimental images capture the actual deformation patterns and typical failure mechanisms, such as cracking of the concrete and yielding of the GiR. The FE simulation results, represented by stress and strain distributions, reveal similar failure patterns, demonstrating that the model accurately replicated the load transfer mechanisms and failure processes within the specimens. The validation results underscored that the FE model is capable of reliably predicting the load-bearing capacity and deformation

characteristics of TCC specimens, with only minor deviations observed in the post-peak response phase. These findings affirm the suitability of the FE model for future analyses, including the design and optimization of TCC connections.

Parametric Study and Discussion

A parametric analysis of the TCC connectors was conducted to identify the most sensitive parameters, based on the validated model. The GL series examined variations in the threaded rod diameter and length to facilitate parametric extension and address the differences within the experimental parameters. Conversely, the RG series focused on the length for similar parametric expansion to bridge the gaps observed in the experimental data. The parameters and the outcomes of the FE analysis are summarized in Table 7.

Table 7 shows the FE analyses, specifically reporting the ultimate shear capacity, yield capacity, and ductility factor.

Table 7. Finite Element Analysis Results from Parameter Analysis

	1					
Specimen	F _{max} (kN)	∆ _u (mm)	F_{y} (kN)	Δ_y (mm)	K (kN/mm)	η
GL10-150	75.3	18.1	36.6	2.5	29.8	8.8
GL10-170	83.7	20.8	38.3	3.1	16.2	7.6
GL10-190	85.5	23.2	38.7	3.2	15.0	8.0
GL10-210	89.3	24.9	39.4	3.5	12.8	8.0
GL12-150	75.2	26.8	38.3	3.2	24.5	8.3
GL12-170	80.3	27.7	37.4	2.6	21.0	10.5
GL12-190	82.2	28.2	39.6	3.7	19.7	7.5
GL12-210	85.6	28.2	40.5	4.1	15.8	6.7
GL16-150	130.9	29.8	75.6	3.5	45.7	8.3
GL16-170	136.7	29.9	76.8	3.8	43.6	7.8
GL16-190	142.5	31.2	77.8	4.0	41.2	7.8
GL16-210	148.9	32.2	79.1	4.4	41.2	7.2
RG12-50-150	123.6	1.68	113.1	1.0	140.1	1.6
RG12-50-170	121.9	2.0	111.9	1.0	140.0	1.9
RG12-50-190	123.7	1.6	113.1	1.0	140.0	1.6
RG12-50-210	123.7	1.6	113.2	1.0	140.0	1.6
RG12-100-150	295.5	1.8	263.0	0.8	395.4	2.0
RG12-100-170	255.7	1.9	227.5	0.9	333.9	2.1
RG12-100-190	223.1	2.1	199.7	1.0	262.0	2.0
RG12-100-210	194.0	2.1	174.4	1.0	209.4	1.9
RG12-150-150	299.0	2.2	263.8	1.0	339.0	2.1
RG12-150-170	256.7	2.3	226.6	1.1	267.0	2.0
RG12-150-190	222.7	2.4	197.5	1.2	211.1	1.9
RG12-150-210	195.6	2.5	174.0	1.3	169.6	1.8

Note: The label name GL-10-150 refers to GL Series - GiR Diameter - GiR Length, and RG12-100-150 refers to RG Series - Notch Size - GiR Length. F_{max} is the ultimate shear capacity, Δ_{u} is the slip corresponding to ultimate shear capacity, F_{y} is the yield load, Δ_{y} is the slip corresponding to ultimate shear capacity, K is the stiffness, and η is the Ductility factor.

Stiffness calculations were performed according to the methodology outlined in EN 26891(1991), which is shown in Eq. 3,

$$K = \frac{0.4F_{\text{max}} - 0.1F_{\text{max}}}{\Delta_{0.4} - \Delta_{0.1}} \tag{3}$$

where $\Delta_{0.4}$ and $\Delta_{0.1}$ are the slip (pre-peak) corresponding to 0.4 F_{max} and 0.1 F_{max} , respectively.

The yield point was identified using the geometrograph method, as visually demonstrated in Fig. 11. It was defined as the displacement at the loading point corresponding to the instance where the declining load reaches 85% of the peak ultimate load. The ductility factor was calculated as the ratio of ultimate displacement to yield displacement, as shown in Eq. 4.

$$\eta = \frac{\Delta_u}{\Delta_v} \tag{4}$$

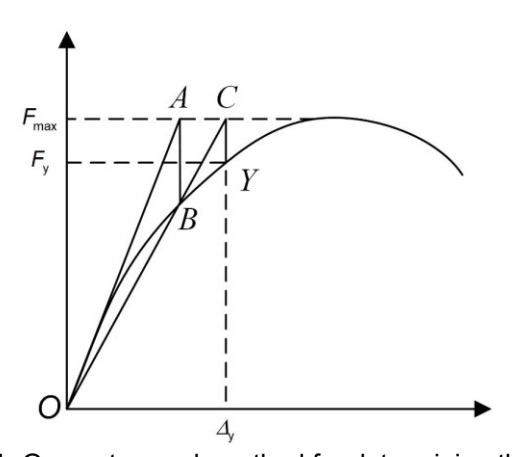


Fig. 11. Geometrograph method for determining the yield point

GL Series

Figure 12(a) presents the load-slip curves for various specimen codes of GL series specimens. A clear trend emerges demonstrating that an increase in the nominal diameter of the reinforcing rod correlates with enhanced load-carrying capacity. For example, the GL16-170 specimen consistently exhibits a higher load compared to the GL10-170 specimen. This phenomenon is primarily attributed to the larger cross-sectional area of the rods with greater diameters, which inherently provides increased resistance to the induced shear forces. The embedment length significantly influences the performance of connection. Specimens incorporating longer embedment lengths, exemplified by the comparison between GL10-210 and GL10-170, consistently demonstrate superior load-carrying capacity. This improvement is due to the expanded bond area facilitated by the increased embedment length, promoting a more effective load transfer mechanism between the reinforcement and the surrounding concrete matrix.

Figure 12(b) compares the stiffness and load-carrying capacity for different nominal diameters of the rod. It is important to highlight that the figure employs bar charts to depict stiffness values while utilizing dotted line graphs to represent load capacities, a convention that is consistently applied throughout the study. The results demonstrate that both stiffness and load-carrying capacity exhibit a positive correlation with the rod diameter. The derived regression equation indicates a power-law relationship between the

rod diameter and the load-carrying capacity, suggesting that the load-carrying capacity increases at an accelerating rate relative to the diameter. This non-linear relationship can be attributed to the synergistic effects of an enlarged cross-sectional area and an optimized distribution of bond-shear stress. Furthermore, the embedment length is identified as a critical factor influencing the connection behavior. Comparative analysis of specimens with differing embedment lengths, such as GL10-210 versus GL10-170, revealed that longer embedment lengths correspond to enhanced load-carrying capacity. This improvement is primarily due to the increased bond area between the reinforcement and the surrounding concrete, which facilitates more efficient load transfer. Figure 12(c) illustrates the influence of embedment length on stiffness and load. The results show that both parameters increase with embedment length, although the rate of increase in load-carrying capacity appears to plateau beyond a certain embedment length threshold. This diminishing return effect may be explained by the reduced contribution of additional embedment length to bond strength, potentially caused by stress concentration at the terminal region of the embedment zone.

RG Series

As shown in Fig. 13 (a), the load-displacement curves exhibited an initial steep ascent followed by a gradual plateau. In the early stages of deformation, the load rose sharply with displacement, which can be attributed to the robust interfacial bonding between concrete, timber, and reinforcing bars, which collectively contribute to high structural stiffness. As displacement progressed, localized microcracking or interfacial slippage gradually developed, leading to a reduction in overall stiffness. Nevertheless, the dowel-and-notch connection system continued to sustain significant load-bearing capacity due to its mechanical interlock mechanism. Figure 13 (b) compares stiffness and load-bearing capacity across varying notch dimensions. The findings revealed that a 100 mm notch size offered superior stiffness and load-bearing performance compared to both 50 mm and 150 mm configurations. The 100 mm notch size was optimized by balancing mechanical interlock efficiency and timber material integrity, as elucidated by contact pressure (CPRESS, Fig. 14) and principal stress (S₁₁, Fig. 15) distributions for specimens with 170 mm embedment length.

50 mm notch (RG12-50-170): CPRESS exhibited a narrow distribution with a maximum of 12.3 MPa, indicating insufficient mechanical interlock between timber and concrete—only localized contact occurred, limiting load transfer efficiency (Fig. 14). Correspondingly, the S_{11} distribution showed low peak stress (14.5 MPa) and limited stress propagation into timber (Fig. 15), meaning that timber contributed minimally to composite action, resulting in premature slip and low stiffness (consistent with Fig. 13 (b)).

150 mm notch (RG12-150-170): CPRESS peaked at 49.9 MPa with severe local concentration (Fig. 14), which induced excessive compressive principal stress (S_{11} < -26.8 MPa, Fig. 15) at the timber-notch interface. This compressive stress far exceeded the tangential compressive strength of glulam (5.05 MPa, Table 3), causing timber crushing that disrupted the composite load-transfer mechanism.

100 mm notch (RG12-100-170): CPRESS distributed uniformly with a peak of 79.5 MPa (Fig. 14), ensuring robust mechanical interlock. The principal stress (S_{11} = 16.9 MPa, Fig. 15) remained within timber's elastic range (without exceeding compressive strength), allowing synergistic load sharing between timber and connectors. Thus, the 100 mm notch achieved the highest stiffness and load-bearing capacity by maintaining composite action without timber failure.

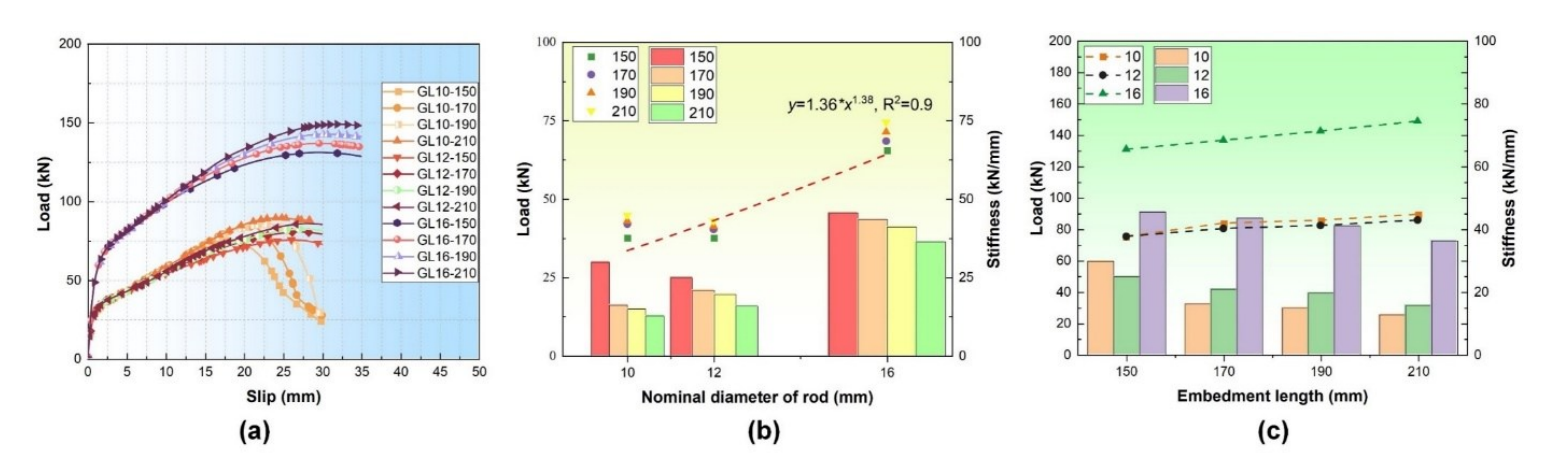


Fig. 12. Parameter analysis of GL series specimens: (a) Load slip curves, (b) comparison of the stiffness and load carrying capacity of GL connections with different diameters, and (c) comparison of the stiffness and load carrying capacity of GL connections with different embedment lengths

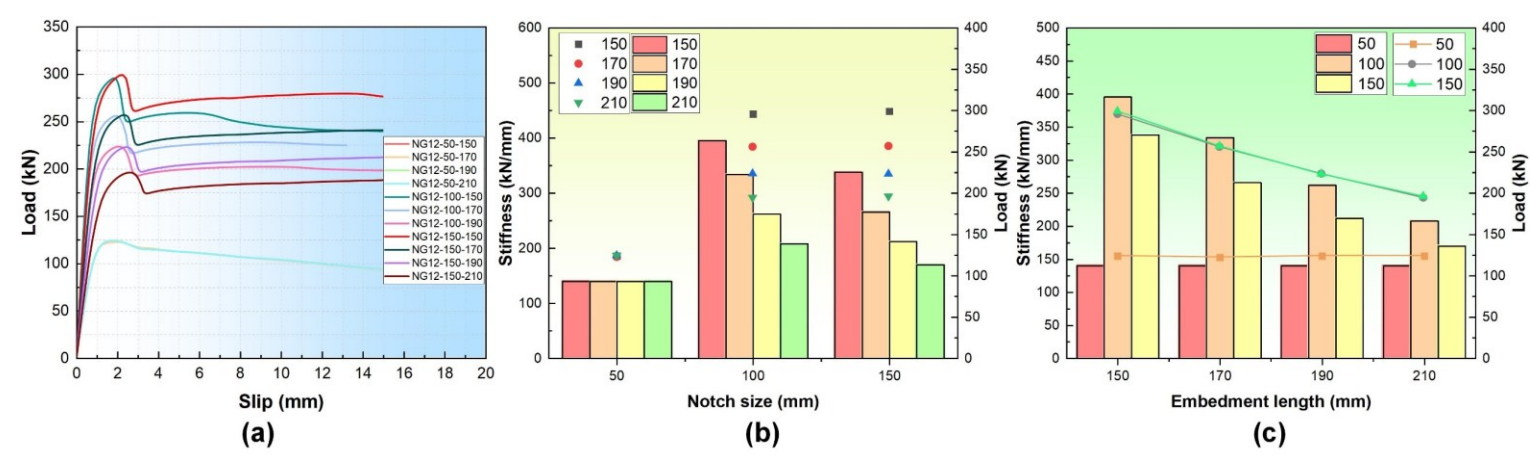


Fig. 13. The results of parameter analysis of RG series specimens: (a) Load slip curves, (b) comparison of the stiffness and load carrying capacity of RG connections with different notch size, and (c) comparison of the stiffness and load carrying capacity of RG connections with different embedment lengths

Figure 12(c) compares the mechanical behavior under different GiR embedment lengths. The results demonstrate that stiffness diminished progressively as the embedment length was increased from 150 mm to 210 mm. Shorter embedment lengths enhanced the confinement effect exerted by both concrete and timber on the reinforcing bar, thereby improving stiffness. However, the load-bearing capacity did not exhibit a strictly decreasing trend with longer embedment lengths. Notably, the 150 mm embedment length achieved the highest load-bearing capacity, which was likely due to enhanced bond strength and anchorage efficiency within a confined zone. Conversely, longer embedment lengths (e.g., 210 mm) still maintained acceptable load-bearing performance by facilitating the formation of a more extensive and stable anchorage system. In summary, the selection of embedment length should be carefully optimized to achieve an appropriate balance between stiffness and load-bearing capacity, tailored to the specific demands of the engineering application.

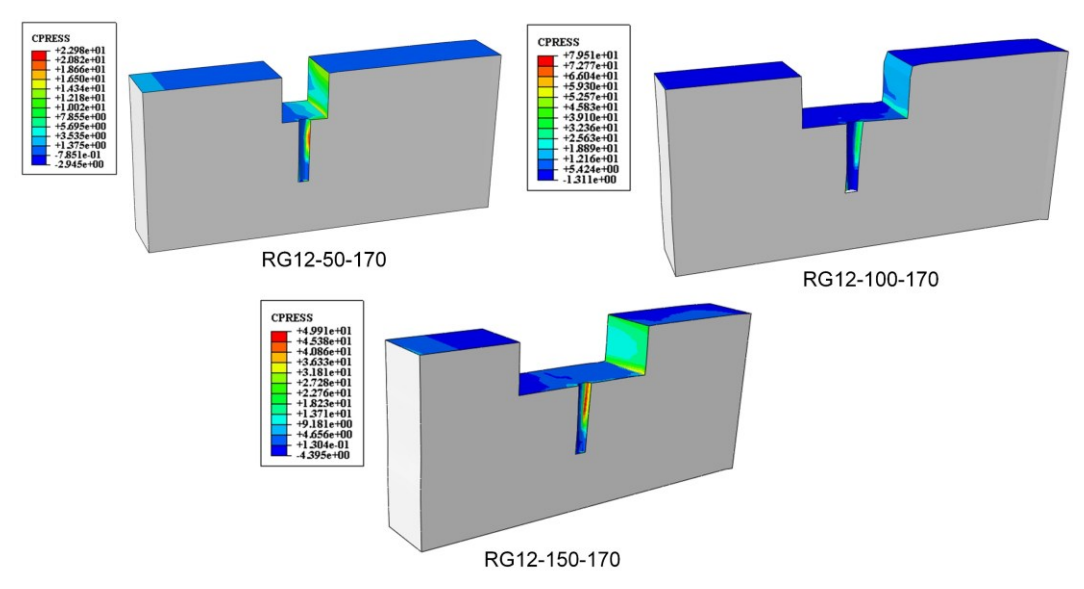


Fig. 14. The contact force distribution at the timber interface

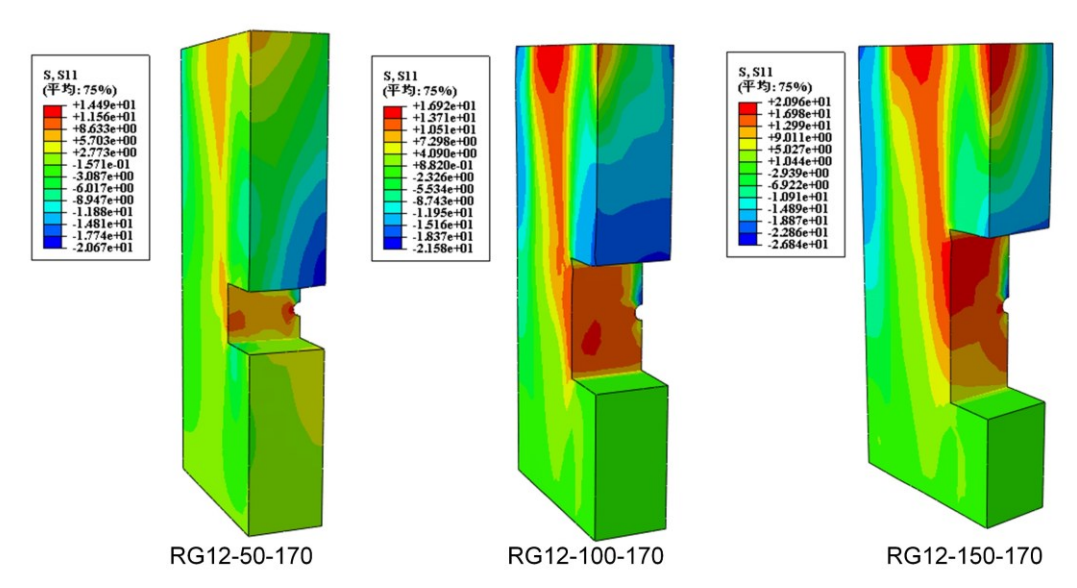


Fig. 15. Distribution of principal stresses in timber

Different Type Connection

The FE parametric analysis results of the TCC connection with GiR and notches exhibited distinct trends across different notch sizes. Concerning load capacity (Fig. 16 (a)), as the notch size was increased from 0 to 50 mm, the load initially exhibited an upward trend. This initial increase was likely attributable to the alleviation of initial stress concentration and enhanced efficiency in load transfer. However, when the notch size surpassed 100 mm, the load reached a plateau and experienced slight fluctuations. This phenomenon can be explained by the progressive reduction in the effective load-bearing area of the connection, where the positive effects of stress redistribution were offset by the escalating damage to the structural integrity. The stiffness initially increased up to a notch size of 100 mm (Fig. 16 (b)), which was likely due to the smaller notch facilitating partial stress concentration alleviation while maintaining the overall structural rigidity. Beyond this threshold, further enlargement of the notch size led to a decrease in stiffness. This reduction was probably attributable to excessive material removal, which diminished the connection's capacity to resist deformation under applied loads.

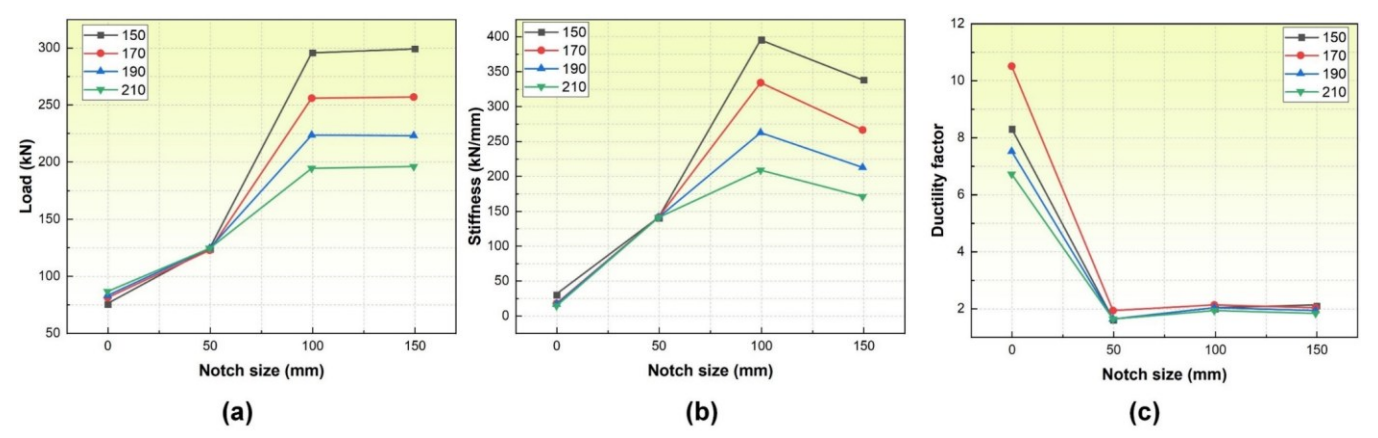


Fig. 16. The results of parameter analysis of different series specimens: (a) Load, (b) Stiffness, and (c) Ductility factor.

In terms of ductility (Fig. 16(c)), the trend was particularly pronounced. The ductility factor exhibited a sharp decrease as the notch size increases from 0 to 50 mm, followed by a continued decline at a reduced rate as the notch dimensions further expand. The initial steep reduction indicates that even minor notching can substantially impair the connection's ductility by introducing stress concentration points that impede plastic deformation. The subsequent more gradual decrease suggests that while additional notch enlargement continues to degrade ductility, the rate of deterioration slows as the connection's inherent deformation capacity becomes significantly compromised.

Prediction of Load Capacity and Recommendations

GL series

Three distinct failure modes were identified through push-out tests and FE simulations, which exhibited strong similarities to the previously reported failure modes of TCC metal connectors (Cao *et al.* 2021b). As shown in Fig. 17, these failure modes correspond to timber embedment crushing, single plastic hinge formation, and double plastic hinge development, respectively.

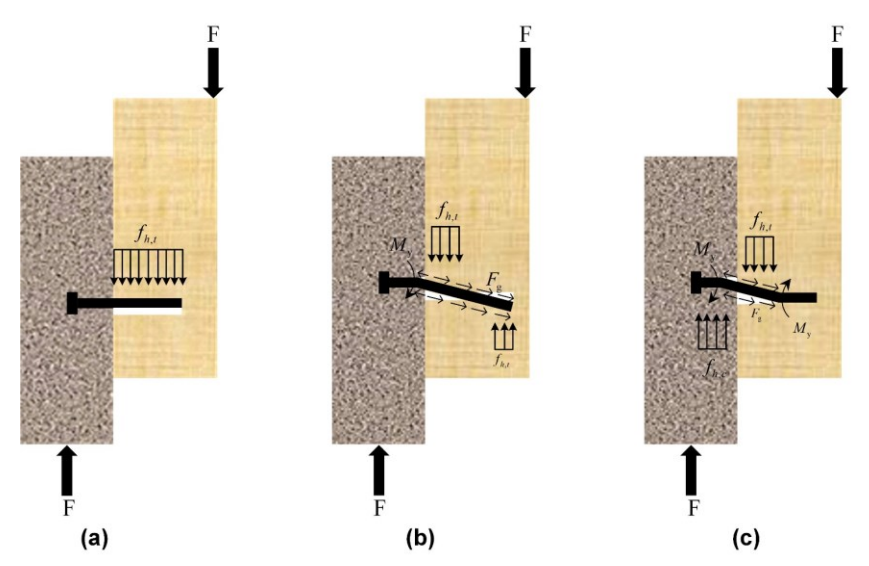


Fig. 17. Mechanical models of typical TCC metal fastener failure: (a) Model I: timber embedment crushing, (b) model II: single-plastic hinge formation, and (c) model III: double-plastic hinge development

The bearing capacity was calculated by Eq. 5,

$$F_{v} = \min \begin{cases} f_{h,t}d_{h}l_{t} \\ f_{h,t}d_{h} \left[2\alpha \sqrt{\frac{M_{y}}{(1+2\alpha)} + \frac{\alpha+1}{2(2\alpha+1)^{2}}} - \frac{l_{t}}{2\alpha+1} \right] + \frac{F_{g}}{4} \\ f_{h,t}d_{h} \sqrt{\frac{4M_{y}}{(1+\alpha)\alpha f_{h,c}d_{h}}} + \frac{F_{g}}{4} \end{cases}$$
(5)

where $f_{h,t}$ is the embedment strength of timber (MPa) and calculated according to Eq. 6, d_h is the drill-hole diameter of GiR in timber (mm), l_t is the length of threaded rod in the timber (mm), $f_{h,c}$ is the embedment strength of GiR in concrete (MPa) and calculated by Eq. 7, as recommended by Dias *et al.* (2018), $\alpha = f_{h,t} / f_{h,c}$, M_y is the yield moment of GiR and calculated by Eq. 8 (Blass and Colling 2015), and F_g is the pull-out capacity of GiR glued in perpendicular adopted by the recommendation by Widmann, as shown in Eq. 9.

$$f_{h,t} = 0.11(1 - 0.01d_h)\rho_k \tag{6}$$

$$f_{\rm h,c} = 4f_{\rm c} \tag{7}$$

$$M_{y} = f_{y,k} d_{h}^{3} / 6 \tag{8}$$

$$F_{\rm g} = 0.045 \left(\pi l_{\rm t} d_{\rm h}\right)^{0.8} \tag{9}$$

where ρ_k is the density of timber (kg/m³), f_c is compression strength of concrete, and $F_{y,k}$ is the equivalent yield strength taken as 90% of the ultimate tensile strength of the threaded rod (MPa).

The comparative analysis results are summarized in Table 8. The theoretical model demonstrated a satisfactory predictive capability for the load-bearing capacity of the specimens, with error percentages ranging from 6% to 14%. Thus, the model can effectively estimate the structural performance across various configurations. Overall, the theoretical model is a useful tool for predicting the structural behavior of the specimens, providing a solid foundation for further refinement and application in structural engineering design.

Specimen	F _{max} (kN)	F _{pre} (kN)	Error (%)	Specimen	F _{max} (kN)	F _{pre} (kN)	Error (%)
GL10-150	75.3	70.7	6	RG12-50-150	123.6	123.96	-1
GL10-170	83.7	73.3	12	RG12-50-170	121.9	127.46	-1
GL10-190	85.5	75.8	11	RG12-50-190	123.7	130.96	-1
GL10-210	89.3	78.2	12	RG12-50-210	123.7	134.46	-1
GL12-150	75.2	67.5	10	RG12-100-150	295.5	198.42	32
GL12-170	80.3	70.4	12	RG12-100-170	255.7	202.01	20
GL12-190	82.2	73.2	10	RG12-100-190	223.1	205.51	1
GL12-210	85.6	75.94	11	RG12-100-210	194.0	209.01	-1
GL16-150	130.9	118.3	9	RG12-150-150	299.0	221	26
GL16-170	136.7	121.8	10	RG12-150-170	256.7	221	14
GL16-190	142.5	125.3	12	RG12-150-190	222.7	221	1
GL16-210	148.9	128.6	14	RG12-150-210	195.6	221	-12

 Table 8. Comparison of Numerical Analysis and Predicted Model

RG series

The mechanical model of a typical metallic TCC connector with notches was based on experiments, finite elements, and previous studies (Yeoh *et al.* 2011; Mirshekar and Sadeghian 2025), as shown in Fig. 18. The bearing capacity was calculated by Eq. 10,

$$F_{v} = \min \begin{cases} F_{\text{conc,shear}} = F_{\text{notch}} + F_{\text{GiR}} \\ F_{\text{conc,crush}} = 0.75 f_{c} t h \\ F_{\text{timber,shear}} = f_{s} l_{e} t \\ F_{\text{timber,crush}} = f_{t} t h \end{cases}$$

$$(10)$$

where $F_{\text{con,shear}}$ is the concrete shear resistance, which is composed of two distinct components: the resistance provided by the notch (including both the concrete and timber elements) and the GiR resistance. The detailed calculation is shown in Eq. 11 (Mirshekar and Sadeghian 2025). F_{GiR} is the GiR resistance, which could be derived by Eq. (9). The quantity t is the thickness of the timber, and h is the depth of the notch, as shown in Fig. 2. The parameter f_s is the shear strength of the timber, and l_e is the distance between the timber edge and the notch edge.

$$F_{notch} = [0.0375l_{\rm n} + 0.358L''] \cdot f_{\rm c}t + \frac{ht}{2} \cdot \left(\frac{f_{\rm c} \tan 53^{\circ}}{\tan 53^{\circ} + \cot 53^{\circ}}\right)$$
(11)

where l_n is the length of the notch, as shown in Fig. 2. L^n takes the minimum value between l_n /8 and 20 mm.

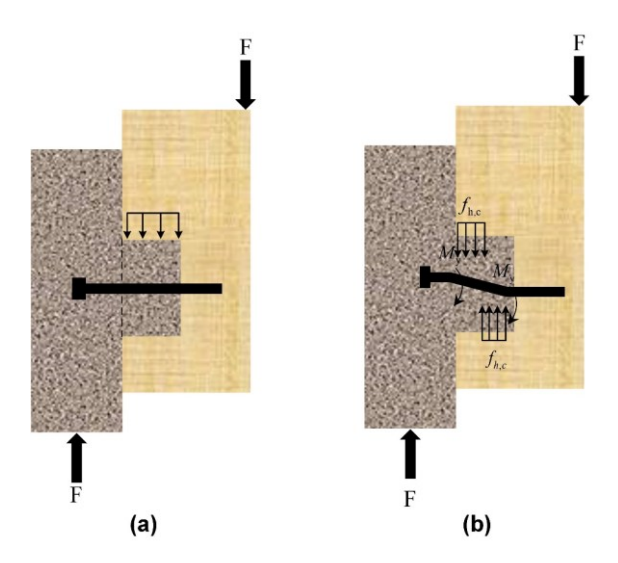


Fig. 18. Mechanical models of RG series TCC connection failure

The comparison results are presented in Table 8. Specimens with a notch length of 50 mm (RG12-50 series), the theoretical predictions closely match the finite element (FE) analysis results, with discrepancies confined within ±1%. This demonstrates that the model reliably estimates the load-bearing capacity when failure occurs predominantly through double-hinge collapse and concrete shear failure. It also shows that variations in embedded length had minimal impact on the predictions. In contrast, for specimens with a notch length of 100 mm (RG12-100 series), the theoretical approach tended to underestimate the actual load-bearing capacity, with errors ranging from 1% up to 32%. This indicates that the current model did not fully account for the effects of embedded length on capacity in this scenario. Similarly, the RG12-150 series exhibits a range of prediction errors, further emphasizing certain limitations of the model under specific conditions. Overall, although the theoretical framework provides reasonable estimates for particular configurations, additional refinement is necessary to improve its predictive accuracy across all test cases.

The theoretical models developed for predicting the load capacity of both GL and RG series connectors demonstrated satisfactory accuracy, with error percentages falling within a range of 6% to 32%. Although these models provided reliable estimations for specific connector configurations, notable discrepancies were observed, highlighting the need for further refinement. In particular, the influence of critical factors such as embedment length and notch size on load transfer mechanisms requires more precise characterization. Future research efforts should focus on enhancing the predictive accuracy of these theoretical models, while also expanding the investigation to include dynamic loading scenarios and long-term performance assessments under various service conditions.

CONCLUSIONS

1. The finite element (FE) model developed demonstrated strong predictive capability in simulating the structural performance of timber concrete composite (TCC) connectors, successfully reproducing experimentally observed load—slip curves and failure modes with high fidelity. The most common failure modes identified were: (1) For the GL

series (no notches): A combination of timber embedment crushing (Model I) and GiR single-plastic hinge formation (Model II) was observed in 80% of specimens. This arose from shear stress concentration at the GiR-timber interface. (2) For the RG series (with notches): Concrete tensile cracking at the notch followed by timber embedment crushing was observed in 75% of specimens. This was due to notch-induced stress redistribution, where concrete failed first in tension before load transferred to timber and GiR. Minor post-peak deviations in the FE model were attributed to localized damage (e.g., micro-cracking in concrete) and simplifications in bonding behavior modeling.

2. The load-carrying capacity and stiffness of connectors without notches (GL series) were effectively improved by increasing the GiR diameter and embedment length. However, beyond a critical embedment length, the rate of stiffness enhancement gradually decreased due to stress concentration occurring at the terminal regions of the embedment zone. For connectors featuring notches (RG series), a notch dimension of 100 mm was found to offer an optimal balance between stiffness performance and load-bearing capacity. Notably, smaller notch sizes led to reduced material interlocking, whereas excessively large notches compromised the overall structural integrity. The embedment length of GiR within the concrete matrix was identified as a critical factor influencing load capacity, where shorter embedment lengths were shown to enhance confinement effects and consequently improve stiffness characteristics.

ACKNOWLEDGMENTS

The authors greatly appreciate the financial support from the National Natural Science Foundation of China (Grant No. 52108253), the Natural Science Foundation of Jiangsu Province, China (Grant No. BK20221387) and the Key Laboratory of Building Structural Retrofitting and Underground Space Engineering (Shandong Jianzhu University), and Ministry of Education (Grant No. MEKL202306).

REFERENCES CITED

Abaqus User Manual (2021). Abaqus/CAE User's Manual.

Ahmadi, B., and Saka, M. (1993). "Behavior of composite timber-concrete floors," *Journal of Structural Engineering* 119(11), 3111-3130.

Azinović, B., Danielsson, H., Serrano, E., and Kramar, M. (2019). "Glued-in rods in cross laminated timber – Numerical simulations and parametric studies," *Construction and Building Materials* 212, 431-441. DOI: 10.1016/j.conbuildmat.2019.03.331

Bedon, C., and Fragiacomo, M. (2017). "Three-dimensional modelling of notched connections for timber–concrete composite beams," *Structural Engineering International* 27(2), 184-196.

Blass, H. J., and Colling, F. (2015). "Load-carrying capacity of dowelled connections," in: *Proceedings of the 48th INTER Meeting*.

Boccadoro, L., and Frangi, A. (2014). "Experimental analysis of the structural behavior of timber-concrete composite slabs made of beech-laminated veneer lumber," *Journal*

- of Performance of Constructed Facilities 28(6), article A4014006.
- Boccadoro, L., Zweidler, S., Steiger, R., and Frangi, A. (2017). "Bending tests on timber-concrete composite members made of beech laminated veneer lumber with notched connection," *Engineering Structures* 132, 14-28. DOI: 10.1016/j.engstruct.2016.11.029
- Bodig, J., and Jayne, B. A. (1982). *Mechanics of Wood and Wood Composites*, Van Nostrand Reinhold Company.
- Cao, J., Xiong, H., and Chen, J. (2021a). "Mechanical performance of timber-concrete bolted connections under cyclic loading," *Structures* 34, 3464-3477. DOI: 10.1016/j.istruc.2021.09.086
- Cao, J., Xiong, H., and Peng, T. (2021b). "Load-carrying capacity analysis for timber-concrete bolted connections considering the effect of steel pads," *Engineering Structures* 247, article 113095. DOI: 10.1016/j.engstruct.2021.113095
- Chen, L., Yang, L., and Xu, K. (2025). "Experimental and numerical research on overall stability of stainless steel-timber composite beams," *Engineering Structures* 331, article 119982. DOI: 10.1016/j.engstruct.2025.119982
- Danielsson, H., Jeleč, M., Serrano, E., and Rajčić, V. (2019). "Cross laminated timber at in-plane beam loading Comparison of model predictions and FE-analyses," *Engineering Structures* 179, 246-254. DOI: 10.1016/j.engstruct.2018.10.068
- Deam, B. L., Fragiacomo, M., and Buchanan, A. H. (2007). "Connections for composite concrete slab and LVL flooring systems," *Materials and Structures* 41(3), 495-507. DOI: 10.1617/s11527-007-9261-x
- Derikvand, M., and Fink, G. (2022). "Bending properties of deconstructable cross-laminated timber-concrete composite floor elements," *Wood Material Science & Engineering* 17(4), 253-260. DOI: 10.1080/17480272.2022.2077658
- Di Nino, S., Gregori, A., and Fragiacomo, M. (2020). "Experimental and numerical investigations on timber-concrete connections with inclined screws," *Engineering Structures* 209, article 109993. DOI: 10.1016/j.engstruct.2019.109993
- Dias, A., Lopes, S., Van de Kuilen, J. G., and Cruz, H. (2007a). "Load-carrying capacity of timber–concrete joints with dowel-type fasteners," *Journal of Structural Engineering* 133(5), 720-727.
- Dias, A. M. P. G., Van de Kuilen, J. W., Lopes, S., and Cruz, H. (2007b). "A non-linear 3D FEM model to simulate timber–concrete joints," *Advances in Engineering Software* 38(8-9), 522-530. DOI: 10.1016/j.advengsoft.2006.08.024
- Dias, A., Skinner, J., Crews, K., and Tannert, T. (2015). "Timber-concrete-composites increasing the use of timber in construction," *European Journal of Wood and Wood Products* 74(3), 443-451. DOI: 10.1007/s00107-015-0975-0
- Dias, A. M. P. G., and Jorge, L. F. C. (2011). "The effect of ductile connectors on the behaviour of timber–concrete composite beams," *Engineering Structures* 33(11), 3033-3042. DOI: 10.1016/j.engstruct.2011.05.014
- Dias, A. M. P. G., Kuhlmann, U., Kudla, K., Mönch, S., and Dias, A. M. A. (2018). "Performance of dowel-type fasteners and notches for hybrid timber structures," *Engineering Structures* 171, 40-46. DOI: 10.1016/j.engstruct.2018.05.057
- Djoubissie, D. D., Messan, A., Fournely, E., and Bouchaïr, A. (2018). "Experimental study of the mechanical behavior of timber-concrete shear connections with threaded reinforcing bars," *Engineering Structures* 172, 997-1010. DOI: 10.1016/j.engstruct.2018.06.084
- EN 26891 (1991). "Timber structures, joints made with mechanical fasteners, General

- principles for the determination of strength and deformation characteristics," European Committee for Standardization, Brussels, Belgium.
- EN 338 (1995). "Structural timber Strength classes," European Committee for Standardization, Brussels, Belgium.
- EN 1992-1-1 (2005). "Eurocode 2 Design of concrete structures Part 1-1: General rules and rules for buildings," European Committee for Standardization, Brussels, Belgium.
- Eslami, H., Jayasinghe, L. B., and Waldmann, D. (2021). "Nonlinear three-dimensional anisotropic material model for failure analysis of timber," *Engineering Failure Analysis* 130, article 105764. DOI: 10.1016/j.engfailanal.2021.105764
- Eslami, H. (2023). "Influence of different end-of-life cycle scenarios on the environmental impacts of timber-concrete composite floor systems," *Proceedings of the 13th World Conference on Timber Engineering (WCTE)*, Oslo, Norway. 2023.
- Fragiacomo, M., and Lukaszewska, E. (2013). "Time-dependent behaviour of timber—concrete composite floors with prefabricated concrete slabs," *Engineering Structures* 52, 687-696. DOI: 10.1016/j.engstruct.2013.03.031
- Gurkšnys, K., Kvedaras, A., and Kavaliauskas, S. (2005). "Behaviour evaluation of "sleeved" connectors in composite timber-concrete floors," *Journal of Civil Engineering and Management* 11(4), 277-282. DOI: 10.1080/13923730.2005.9636358
- Harrach, D., Habashneh, M., and Rad, M. M. (2022). "Reliability-based numerical analysis of glulam beams reinforced by CFRP plate," *Scientific Reports* 12(1), 1-15. DOI: 10.1038/s41598-022-17751-6
- Hassanieh, A., Valipour, H. R., and Bradford, M. A. (2018). "Bolt shear connectors in grout pockets: Finite element modelling and parametric study," *Construction and Building Materials* 176, 179-192. DOI: 10.1016/j.conbuildmat.2018.05.029
- Jankowiak, T., and Lodygowski, T. (2005). "Identification of parameters of concrete damage plasticity constitutive model," *Foundations of Civil and Environmental Engineering* 6(1), 53-69.
- Khaleel Ibrahim, S., Abbas Hadi, N., and Movahedi Rad, M. (2023). "Experimental and numerical analysis of steel-polypropylene hybrid fibre reinforced concrete deep beams," *Polymers* 15(10), article 2340.
- Lee, J., and Fenves, G. L. (1998). "A plastic-damage concrete model for earthquake analysis of dams," *Earthquake Engineering and Structural Dynamics* 27(9), 937-956. DOI: 10.1002/(SICI)1096-9845(199809)27:9<937::AID-EQE764>3.0.CO;2-5
- Ling, Z., Li, Z., Lu, F., Yang, H., Zheng, W., and Zhang, L. (2023). "Flexural strengthening of timber-concrete composite beams using mechanically fastened and externally bonded combining mechanically fastened strengthening techniques," *Journal of Building Engineering* 78, article 107645. DOI: 10.1016/j.jobe.2023.107645
- Ling, Z., Liu, W., Yang, H., and Chen, X. (2018). "Modelling of glued laminated timber joints with glued-in rod considering bond-slip location function," *Engineering Structures* 176, 90-102. DOI: 10.1016/j.engstruct.2018.08.098
- Ling, Z., Zhang, H., Mu, Q., Xiang, Z., Zhang, L., and Zheng, W. (2022). "Shear performance of assembled shear connectors for timber–concrete composite beams," *Construction and Building Materials* 329, article 127158. DOI: 10.1016/j.conbuildmat.2022.127158
- Mascia, N. T., and Nicolas, E. A. (2012). "Evaluation of Tsai-Wu criterion and

- Hankinson's formula for a Brazilian wood species by comparison with experimental off-axis strength tests," *Wood Material Science and Engineering* 7(1), 49-58. DOI: 10.1080/17480272.2012.654820
- Mirshekar, S., and Sadeghian, V. (2025). "Numerical and analytical models for predicting load-carrying capacity of timber–concrete notched connections," *Journal of Structural Engineering* 151(7). DOI: 10.1061/jsendh.Steng-14360
- Mohamadzadeh, M., Rostampour Haftkhani, A., Ebrahimi, G., and Yoshihara, H. (2012). "Numerical and experimental failure analysis of screwed single shear joints in wood plastic composite," *Materials & Design* 35, 404-413. DOI: 10.1016/j.matdes.2011.09.061
- Molina, J. C., Oliveira, C. A. B., Christoforo, A. L., Bôas, D. V., and Calil Junior, C. (2020). "Influence of the bonding of rebar dowel with adhesive on wood–concrete composite specimens," *Proceedings of the Institution of Civil Engineers-Structures and Buildings* 173(12), 904-913.
- Oudjene, M., Meghlat, E. M., Ait-Aider, H., and Batoz, J. L. (2013). "Non-linear finite element modelling of the structural behaviour of screwed timber-to-concrete composite connections," *Composite Structures* 102, 20-28. DOI: 10.1016/j.compstruct.2013.02.007
- Quang Mai, K., Park, A., Nguyen, K. T., and Lee, K. (2018). "Full-scale static and dynamic experiments of hybrid CLT–concrete composite floor," *Construction and Building Materials* 170, 55-65. DOI: 10.1016/j.conbuildmat.2018.03.042
- Rodrigues, J. N., Providência, P., and Dias, A. M. P. G. (2017). "Sustainability and lifecycle assessment of timber-concrete composite bridges," *Journal of Infrastructure Systems* 23(1), article 04016025.
- Serrano, E. (2001). "Glued-in rods for timber structures—An experimental study of softening behaviour," *Materials and Structures* 34, 228-234.
- Shahnewaz, M., Jackson, R., and Tannert, T. (2022). "CLT concrete composite floors with steel kerf plate connectors," *Construction and Building Materials* 319, article 126092. DOI: 10.1016/j.conbuildmat.2021.126092
- Shi, B., Liu, W., and Yang, H. (2021). "Experimental investigation on the long-term behaviour of prefabricated timber-concrete composite beams with steel plate connections," *Construction and Building Materials* 266, article 120892. DOI: 10.1016/j.conbuildmat.2020.120892
- Shi, D., Hu, X., Zhang, J., and Du, H. (2022). "Shear stiffness of notched connectors in glue laminated timber-concrete composite beams under fire conditions," *BioResources* 17(4), 6397-6410. DOI: 10.15376/biores.17.4.6397-6410
- Shirmohammadli, Y., Hashemi, A., Masoudnia, R., and Quenneville, P. (2023). "Numerical modeling investigation of cross-laminated timber connections consisting of multiple glued-in rods," *Structures* 53, 491-500. DOI: 10.1016/j.istruc.2023.04.090
- Tao, H., Shi, B., Yang, H., Wang, C., Ling, X., and Xu, J. (2022). "Experimental and finite element studies of prefabricated timber-concrete composite structures with glued perforated steel plate connections," *Engineering Structures* 268, article 114778. DOI: 10.1016/j.engstruct.2022.114778
- Yeoh, D., Fragiacomo, M., De Franceschi, M., and Buchanan, A. H. (2011). "Experimental tests of notched and plate connectors for LVL-concrete composite beams," *Journal of Structural Engineering* 137(2), 261-269.
- Zeman, M., Sejkot, P., Mikes, K., Fragiacomo, M., and Aloisio, A. (2024). "Glued-in steel plate and screwed connections in timber-concrete composites systems:

Mechanical performance and design implications," *Journal of Building Engineering* 2024, article 110477. DOI: 10.1016/j.jobe.2024.110477

Zhang, L., Zhou, J., and Chui, Y. H. (2022). "Development of high-performance timber-concrete composite floors with reinforced notched connections," *Structures* 39, 945-957. DOI: 10.1016/j.istruc.2022.03.074

Article submitted: July 11, 2025; Peer review completed: June 30, 2025; Revised version received and accepted: October 7, 2025; Published: October 20, 2025.

DOI: 10.15376/biores.20.4.10460-10486

APPENDIX

Specimen group code	F _{max} (kN)	Δu	Fy	Δy	K _{0.1}	η
		(mm)	(kN)	(mm)	(kN/mm)	
GL10-150-D(EN) (1)	64.9	15.1	29.8	2.1	21.2	7.1
GL10-150-D(EN) (2)	75.2	21.7	33.1	2.9	10.0	7.5
GL10-150-D(EN) (3)	75.2	19.3	22.1	3.1	4.5	6.2
Mean	66.8	18.7	28.3	2.7	11.9	7.0
CoV (%)	9.2	14.5	16.2	15.6	58.5	7.9
GL12-170-D(EN) (1)	80.0	26.2	30.7	3.1	6.9	8.6
GL12-170-D(EN) (2)	85.2	29.0	31.7	3.4	4.9	8.4
GL12-170-D(EN) (3)	82.0	21.1	34.3	2.1	15.0	10.0
Mean	82.4	25.4	32.2	2.9	8.9	9.0
CoV (%)	2.6	12.7	4.7	19.2	48.7	7.7
GL16-210-D(EN) (1)	164.5	35.5	78.18	4.03	15.62	8.79
GL16-210-D(EN) (2)	160.9	33.3	75.58	5.93	12.43	5.62
GL16-210-D(EN) (3)	154.5	35.1	77.14	5.21	17.55	6.73
Mean	160.0	34.6	77.0	5.1	15.2	7.1
CoV (%)	2.6	2.6	1.3	15.4	13.8	18.6
RG12-50-D(EN) (1)	146.4	1.3	124.7	0.8	97.6	1.7
RG12-50-D(EN) (2)	117.5	1.5	100.5	0.9	160.3	1.7
RG12-50-D(EN) (3)	124.9	1.9	98.2	0.9	101.3	2.0
Mean	129.6	1.6	107.8	0.9	119.7	1.8
CoV (%)	9.4		11.1	7.1	24.0	7.9
RG12-100-D(EN) (1)	260.1	1.7	224.7	1.2	185.8	1.7
RG12-100-D(EN) (2)	247.7	2.0	204.2	1.1	200.9	2.0
RG12-100-D(EN) (3)	208.4	2.5	167.7	1.9	152.5	2.5
Mean	238.7	2.1	198.8	1.4	179.7	1.6
CoV (%)	9.2	15.1	11.8	26.8	11.2	15.5
RG12-150-D(EN) (1)	278.1	2.1	222.8	1.4	185.4	1.5
RG12-150-D(EN) (2)	235.2	2.0	217.7	1.5	147.0	1.3
RG12-150-D(EN) (3)	244.6	2.5	219.6	1.3	215.8	1.9
Mean	252.6	2.2	220.0	1.4	182.7	1.6
CoV (%)	7.2	9.4	0.9	6.4	15.4	14.3

Notes: F_{max} = the ultimate load; Δu = displacement corresponding to ultimate load; F_y = the yield load was calculated by the method in Fig 11; Δy = displacement corresponding to yield load; $K_{0.1}$ = Stiffness; η = ductility.

